Carbon 155 (2019) 147–154

Contents lists available at ScienceDirect

Carbon

journal homepage: www.elsevier.com/locate/carbon

# The synthesis of $Co_3O_4$/C composite with aloe juice as the carbon aerogel substrate for asymmetric supercapacitors

Qinwen Yin [a], Liwen He [b], Jiqiong Lian [a], Jingjing Sun [a], Shengfu Xiao [a], Jinjin Luo [b], Dongya Sun [a, *], An Xie [a], Bizhou Lin [b]

[a] Key Laboratory of Functional Materials and Applications of Fujian Province, School of Materials Science and Engineering, Xiamen University of Technology, Xiamen, 361024, PR China

[b] Fujian Key Laboratory of Photoelectronic Functional Materials, College of Materials Science and Engineering, Huaqiao University, Xiamen, 361021, PR China

ARTICLE INFO

*Article history:*
Received 16 June 2019
Received in revised form
6 August 2019
Accepted 20 August 2019
Available online 22 August 2019

*Keywords:*
$Co_3O_4$
Aloe vera
Interface
Asymmetric capacitor
Hierarchical structure
Bio-carbon substrate

ABSTRACT

Transition metal oxide (TMO)-based 3D hollow nanocomposites with a high loading capacity, large specific surface area, and good dispersity have gained considerable attention for energy-related applications. The controllable fabrication of TMO-based hollow nanostructures with adequate mass transfer channels through a simple and eco-friendly method is highly desirable. Herein, 3D net-like $Co_3O_4$/C composites were solvothermally fabricated and calcined using aloe juice as a novel carbon substrate. The as-prepared material showed a specific capacitance of 1345.2 F $g^{-1}$ at 1 A $g^{-1}$ and excellent charge −discharge stability with capacitance retention of 92.7% after 10000 cycles. Moreover, an asymmetric supercapacitor composed of an ALC-700 positive electrode and an active-carbon negative electrode exhibited a high energy density of 68.17 Wh·$kg^{-1}$ at 549 W $kg^{-1}$ and excellent cycling performance. We report the first use of carbonized aloe juice as a carbon matrix to obtain a 3D hierarchical porous structure for energy devices. The proposed method of aerogel can be generalized to utilize the juices of other fruits, sugarcane, and various plants.



## 1. Introduction

Given recent developments in hybrid electric vehicles (HEVs) and modern portable electronics (MPEs) and the potential surge in future micro- and nanosystems, many researchers have focused on new electrode materials for advanced energy-storage devices [1–3]. Electrochemical capacitors (ECs) are regarded as a promising energy-storage devices due to their high specific energy density, sustainability, long cycling life, and low cost [4,5]. Transition metal oxides (TMOs), carbonaceous materials, and conducting polymers are three major types of electrode materials used in ECs. TMOs and their hybrids commonly feature high theoretical specific capacitance and are ideal electrode materials for pseudocapacitors because they can provide rich nanostructures with hierarchical pores and various oxidation states for efficient interfacial redox reactions [6–8]. However, TMOs also present a number of disadvantages, such as low electrical conductivity, inadequate mass transport, and critical capacity fading at high current densities.

Several efforts have been made to address these shortcomings and bridge the performance gap of these materials, such as accurately designed nanostructures and hybridization with carbonaceous materials [9–12]. Several novel nanostructured TMOs with specifically tailored shapes and morphologies, such as $Co_3O_4$ with 0D nanocrystals [13,14], 1D nanowires [15], 2D nanosheets [16], and 3D microstructures [17–19], have been reported in previous studies, 3D and hollow microstructures with hierarchical pores showed improved functional characteristics and surface areas but insufficient electric conduction. Carbon-based hybrid materials possess high electrical conductivity and electrochemical stabilities, but their capacitance requires further improvement. The synthesis of most carbon-based materials typically involves complex and expensive procedures, which makes the large-scale use of many novel carbon nanomaterials, such as graphene and carbon nanotubes, relatively impractical [20–22]. Therefore, synthesizing inexpensive and effective carbon materials via facile and environment-friendly strategies is highly desirable. Recent

* Corresponding author.
*E-mail address:* 2013123205@xmut.edu.cn (D. Sun).

https://doi.org/10.1016/j.carbon.2019.08.060
0008-6223/

research has shown that biological tissues or molecules can be used as templates for synthetic nanomaterials and those biological enzymes can be used to induce and promote redox reactions [23–26]. Carbon from biomass can duplicate the detailed microstructure of natural species and provide a sufficient conductive network, so as to serve as low-cost carbon source, catalyst, and catalyst support for carbon-based nanomaterials [27–32].

In previous work, we demonstrated the use of cotton, ramie, and sorghum stalk as bio-templates for eco-friendly TMO/C composites exhibiting enhanced capacitance and conductivity, which can be attributed to the enhanced dispersity and conductivity of the resulting materials [14,17,33–39]. However, a large disparity between the experimental results and theoretical capacitance of cobalt oxide could still be observed because of insufficient mass and charge transport due to the rigid carbon fiber skeleton of the biomass. Herein, we introduce the use of aloe juice as a carbon matrix to synthesize a novel net-like $Co_3O_4$/C composite (ALC) with hierarchical pores for ECs using an eco-friendly and economical method. Our special design has a number of merits. First, aloe vera is a common perennial evergreen herb, and its derivatives are widely used in the food, beauty, health care, medicine, and other industries [40,41]. The use of aloe juice as a special carbon source offers great significance for the application of electrochemical devices and can be generalized to the juices of other fruits, sugarcane, and various plants. Second, the gel properties of aloe juice can fabricate a variable structure after carbonization, thereby providing new insights into the design of promising carbonaceous carriers with hierarchical porous and high dispersion, which can facilitate quick charge movement and provide numerous active sites in the dynamic redox process. Third, the as-formed interface between active material and carbonaceous matrix provides good contact and could offer high recyclability in charge/discharge reactions. Most importantly, in the proposed electrode design, all of the functions of each component are effectively utilized and synergistic effects could be realized. The specific capacitance of the proposed biomorphic hybrid is 1345.2 $F\,g^{-1}$ at 1 $A\,g^{-1}$, and its charge–discharge stability is relatively high with capacitance retention of 92.7% after 10000 cycles. The as-assembled asymmetric capacitors (ASC) produced a maximum energy density of 68.17 $Wh\cdot kg^{-1}$ at a power density of 549 $W\cdot kg^{-1}$ and maintained an energy density of 21.39 $Wh\cdot kg^{-1}$ at 5.5 $kW\cdot kg^{-1}$. To the best of our knowledge, this comprehensive performance is among the best to date for applying $Co_3O_4$/C hybrid as electrode in ASC devices.

## 2. Experimental section

### 2.1. Sample preparation

The preparation protocol of the ALC is illustrated in Fig. 1a. Aloe vera was peeled off and the juice was extracted. The juice was freeze-dried and pre-carbonized at 400 °C under an Ar atmosphere for 0.5 h. ALC was then synthesized via a solvothermal route. Exactly 1.5 g of the as-prepared carbon material was immersed in 50 mL of 1 M $Co(NO_3)_2\cdot 6H_2O$ (Sinopharm Group Chemical Reagent Co., Ltd.) of ethanol solution, and the mixture was sonicated for 20 min. The dispersed solution was transferred to a 100 mL autoclave and allowed to react for 12 h at 180 °C. The products of solvothermal reaction were filtered, washed, dried, and annealed for 1 h in a tubular furnace at 500, 600, 700, and 800 °C, and the as-prepared samples were thereafter denoted as ALC-500, ALC-600, ALC-700, and ALC-800, respectively. For comparison, a pristine $Co_3O_4$ sample was also synthesized by subjecting $Co(NO_3)_2\cdot 6H_2O$ to the same process without using carbonized aloe juice (CAJ).

### 2.2. Materials characterization

X-ray diffraction (XRD) patterns were collected at ambient temperature on a Rigaku Smart Lab instrument. Raman spectra were obtained in the range of 300–2000 $cm^{-1}$ on a LABRAM HR-800 spectrometer with a 532 nm laser as an excitation source. Field-emission scanning electron microscopy (FE-SEM) images were obtained using a Zeiss Sigma 500 microscope. Transmission electron microscope (TEM) images were taken using an FEI Talos F200S microscope at an accelerating voltage of 200 kV. Specific surface areas and porosity were measured on a Quantachrome Autosorb-iQ instrument at the liquid-nitrogen temperature using ultrapure $N_2$ gas as the adsorbate. X-ray photoelectron spectroscopy (XPS) measurements were performed on a VG Escalab MK II spectrometer (Scientific Ltd., UK) with a non-monochromatic Al Kα X-ray source (1486.6 eV). The infrared spectra (IR) were measured on a Nicolet 470 FT-IR spectrophotometer with KBr pellets in the 4000–400 $cm^{-1}$ region.

### 2.3. Electrochemical measurements

The products were kept in a CHI 760E electrochemical condition and LAND CT2001A cell keeping instruments in the ranges of voltage of 0–0.6 V and 0–1.5 V. The experiment electrode was well-prepared by active materials, acetylene black and polytetrafluoroethylene coated on Ni foam with a mass ratio of 80: 10: 10. In the survey of electrochemical impedance spectroscopy (EIS), the frequency range was reduced from 100 kHz to 10 mHz. In the third electrode system, the well-prepared activate material, platinum foil and Hg/HgO electrode were took respectively as the working, counter and reference electrode. In the second electrode system, active material (ALC) and active carbon materials (i.e. active carbon (AC) and CAJ) with the same weight were assembled as a asymmetric/symmetric electrodes for the evaluation of further application. All the measurements of electrochemistry are surveyed in 6 mol $L^{-1}$ KOH aqueous electrolyte, and the load mass of each electrode is 3–5 mg $cm^{-2}$.

## 3. Results and discussion

### 3.1. Structural and morphological studies of composites

The fabrication protocol of ALC electrodes, the details of which are listed in the experimental section, is illustrated in Fig. 1a. First, a bead-like carbon frame is formed by peeling the aloe vera, homogenization, freeze-drying, and pre-carbonization at 400 °C (Fig. 1b **and** S1a). The obtained carbon substrate is then impregnated with an aqueous solution of $Co(NO_3)_2$ to form a uniform coating of an amorphous $Co_3O_4$ layer on the carbon surface. When the aloe vera is immersed into the precursor solution, the hydroxyl-rich aloe emodin, besides glucose and mannose (Fig. 1b), and $Co^{2+}$ are transformed into carbon and $Co^{3+}$ via a redox reaction in the hydrothermal reactor, thereby forming $Co_3O_4$. Subsequently, Co-containing nanocrystals are evenly bonded onto the carbon matrix through oxygen-rich groups (Fig. 1c). The ALC composites form a multilevel interspatial reticulate structure after post-annealing at 700 °C in Ar gas (Fig. 1d), similar to the morphology of CAJ (Fig. S1a). Interesting transformations were observed during heat treatment under different temperatures of 500, 600, 700, and 800 °C for 1 h, and the corresponding products were denoted ALC-500, ALC-600, ALC-700, and ALC-800 respectively (Fig. S1b–**1d**).

The TEM image in Fig. 1e shows that the $Co_3O_4$ nanocrystals have a diameter of several nanometers and are evenly anchored on the amorphous carbon material, thus suggesting remarkable dispersivity and porous characteristics. The high resolution TEM (HR-

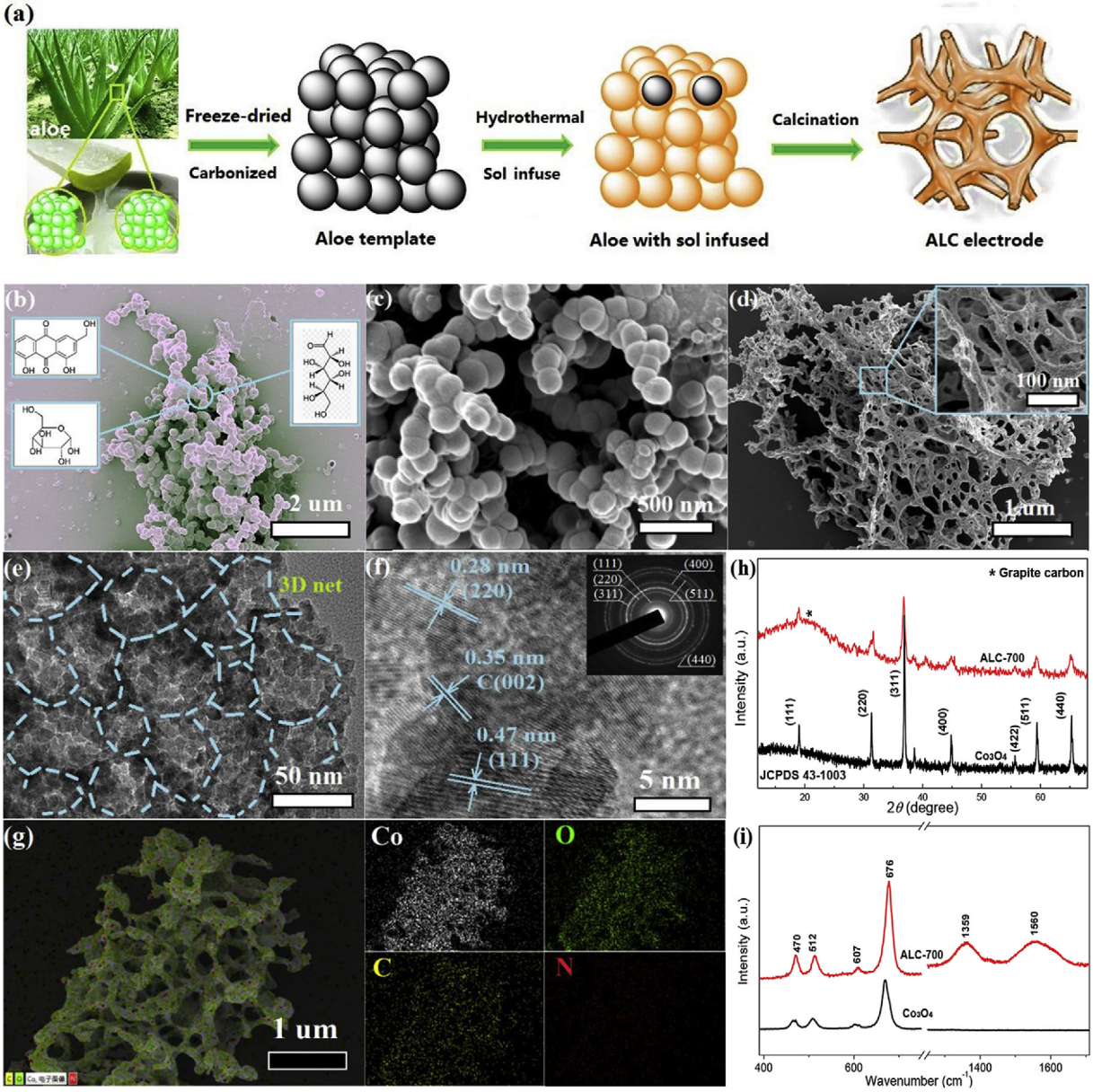


**Fig. 1.** (a) Preparation of ALC electrodes. (b–d) SEM images of the freeze-dried aloe juice, the hydrothermal product, and the ALC-700 composite. (e–g, inset) TEM, HR-TEM, SAED, and EDS mapping of ALC-700. (h) XRD patterns and (i) Raman spectra of ALC-700 and $Co_3O_4$.

TEM) image in Fig. 1f shows the structure of the as-synthesized material; the $Co_3O_4$ layer is clearly polycrystalline, as shown by the selected area electron diffraction (SAED) image in the inset of Fig. 1f. Interplanar spacings of about 0.47 and 0.28 nm, corresponding to the {111} and {220} lattice planes of $Co_3O_4$, as well as an interlayer spacing of 0.35 nm, corresponding to the {002} plane of graphitic carbon, were observed. The distributions of Co, O, C, and N differed among the ALCs (Fig. 1g **and** Table S1). Aloe vera consists of C, O, and N, which suggests that a higher processing temperature can lead to lower C and N contents. The existence of conductive C and N derived from the biomass was recently proposed to be beneficial to the pseudocapacitance of carbonaceous materials [42–44].

The XRD patterns of the ALCs and pristine $Co_3O_4$ are shown in Fig. 1h and S2. All of the diffraction peaks of the products could be well indexed to the (111), (220), (311), (400), (422), (511), and (440) planes of cubic spinel $Co_3O_4$ (JCPDS 43-1003) and correspond to the indices of the SAED rings. Inconspicuous peak at about 20° could be ascribed to amorphous graphitic carbon in the patterns of the ALC-700. And the peak of the graphitic carbon is not obvious gradually with the temperature ascends (Fig. 2S). The existence of carbon could also be proven by the Raman spectra of the samples (Fig. 1i **and** Fig. S3). The four peaks found at around 472, 512, 607, and 676 $cm^{-1}$ on Raman spectra could respectively be attributed to the $E_g$, $F^1_{2g}$, $F^2_{2g}$, and $A^1_g$ modes of cubic $Co_3O_4$ [14,45,46]. The two peaks at 1359 and 1560 $cm^{-1}$ could be attributed to the D- and G-bands of the carbon materials, while no corresponding peaks were detected for $Co_3O_4$ [47]. Differential scanning calorimetry/thermogravimetric analyses (DSC/TG) revealed carbon contents of 12.79 wt%, 7.89 wt%, and 4.19 wt% in ALC-600, ALC-700, and ALC-800, respectively (Fig. S4). These values are consistent with those provided Table S1, suggesting that most of the aloe was oxidized and carbonized during annealing at 800 °C.

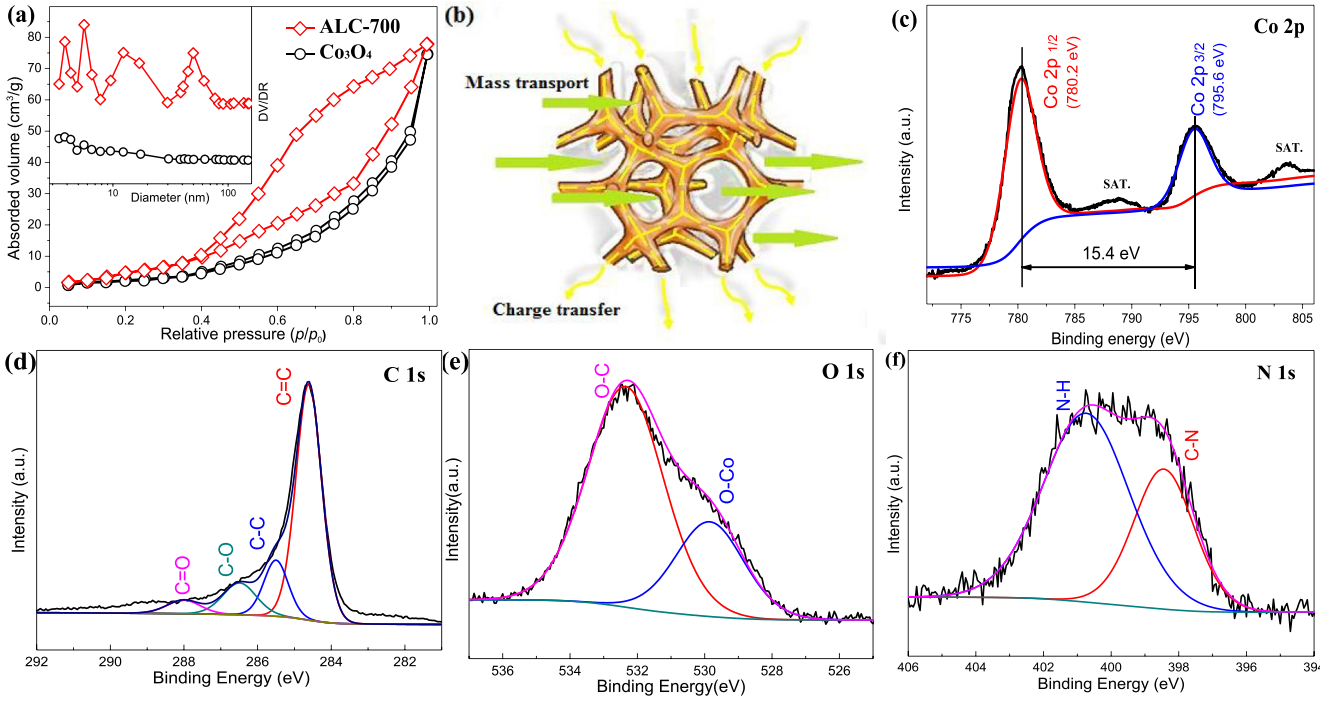


**Fig. 2.** (a) $N_2$ adsorption–desorption isotherm and (inset) related pore size distribution, (b) schematic of mass transport, and XPS spectra of (c) Co 2p, (d) C 1s, (e) O 1s, and (f) N 1s of ALC-700.

### 3.2. $N_2$ adsorption–desorption isotherm and XPS analysis

The $N_2$ adsorption–desorption isotherms of ALC-700 and $Co_3O_4$ in Fig. 2a reflect a typical type-IV isotherm with a hysteresis loop in the $P/P_0$ range of 0.40–1.0, which indicates mesoporous characteristics [48]. Four peaks ranging from 3 nm to 100 nm, which the average pore is 5.31 nm, are found in the pore size distribution curve of ALC-700 which revealing the hierarchical mesoporous properties of the annealed products. The BET specific surface areas of the ALCs (351.1, 413.4, 727.6, and 439.8 $m^2 g^{-1}$) are much larger than that of pristine $Co_3O_4$ (10.8 $m^2 g^{-1}$) (Fig. S5 and Table S2), which is probably due to the unique nanostructure inherited from the bio-carbon matrix. The large pore diameter and volume offered by such hierarchical mesoporous architecture can provide pathways for mass transport and accommodate the requirements of possible volume expansion during electrochemical reactions (Fig. 2b). The as-fabricated structure can also provide sufficient interfacial contact between the active material and electrolyte to promote electron transport and avoid pulverization of the electrode [42]. The XPS patterns of ALC-700 in Fig. 2c–2f confirm that the products contain Co, C, N, and O. The characteristic peaks of C, O, and N could be attributed to the functional groups of aloe juice, corresponding to the IR spectra (Fig. S6). The bond between carbon and $Co_3O_4$ was evidenced by the presence of Co–O signals in the XPS and IR spectra [17]. In the spectrum of Co 2p (Fig. 2c), Co $2p_{3/2}$ and Co $2p_{1/2}$ peaks with band energies (B.E.) of 780.2 and 795.6 eV are consistent with the B.E. of $Co^{3+}$ in $Co_3O_4$ [48]. The higher B.E. splitting out into two peaks of 780.7 and 796.1 eV could be ascribed to the $2p_{3/2}$ and $2p_{1/2}$ of $Co^{2+}$ in $Co_3O_4$. Moreover, the weak 2p satellite features found at 787.9 and 804.5 eV are attributed to typical CoO satellites [16]. Spin orbit splitting between the two peaks at 15.4 eV also confirms the existence of $Co^{2+}$ and $Co^{3+}$ species [45,49].

### 3.3. Electrochemical properties

We evaluated the electrochemical energy-storage performance of the products as anode materials for ECs in three-electrode systems. The cyclic voltammetric (CV) curves of the ALCs and CAJ were measured in the window potential of 0–0.6 V (vs. Hg/HgO). As revealed in Fig. 3a, the ALCs show a pair of redox peaks, thus suggesting that their measured capacitance mainly results from the surface Faradaic reactions of Co ions [50]:

$$Co_3O_4 + H_2O + OH^- \Leftrightarrow 3CoOOH + e^- \quad (1)$$

$$CoOOH + OH^- \Leftrightarrow CoO_2 + H_2O + e^- \quad (2)$$

In Fig. 3b, the CV curves of ALC-700 show similar profiles at different scan rates, thus revealing high rate capabilities and reversible Faradaic reactions between the active material and electrolyte. These findings indicate the good rate performance of the electrode material [17,31–33]. Fig. 3c shows the galvanostatic charge–discharge (GCD) curves of the samples. The specific capacitance can be calculated according to the following equation:

$$C = (I\Delta t)/(m\Delta V), \quad (3)$$

where $C$ is the specific capacitance ($F \cdot g^{-1}$), $I$ is the charge/discharge current (A), $\Delta t$ is the discharge time (s), $\Delta V$ is the potential change during the discharge process (V), and $m$ is the mass of the active material loaded on the working electrode in a three-electrode system (g). ALC-600, ALC-700, and ALC-800 had longer GCD times than pristine $Co_3O_4$, and the specific capacitances of these samples at 1 A $g^{-1}$ are 691.3, 1345.6, 780.2, and 40.0 F $g^{-1}$, respectively, which could be attributed to the introduction of bio-carbon and good dispersion of nanocrystals throughout the well-defined structure of the matrix. The electrochemical property of ALC-700

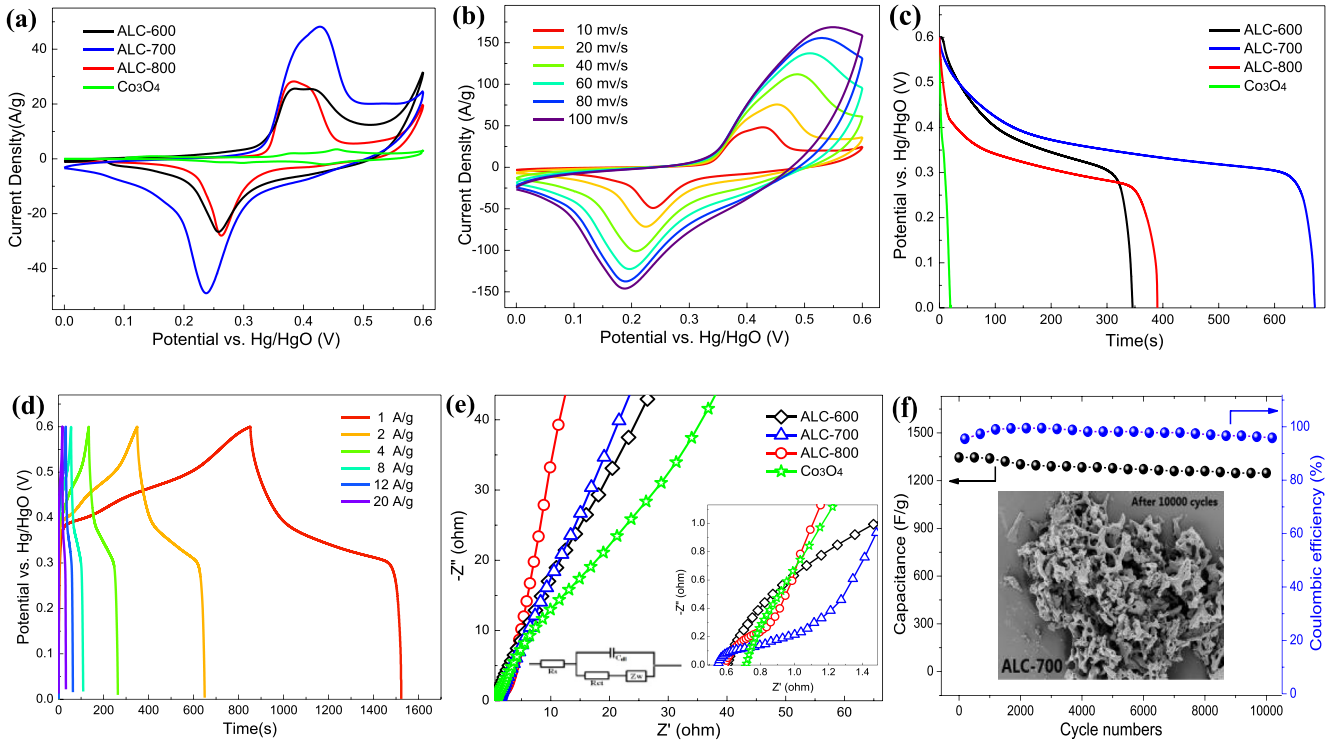


**Fig. 3.** (a) CV curves of samples in 6 M KOH solution at a scan rate of 10 mV $s^{-1}$. (b) CV curves of ALC-700 at various scan rates. Galvanostatic charge–discharge curves (c) of the samples at 1 A $g^{-1}$ and (d) of ALC-700 at various current densities. (e) Nyquist plots of the samples. (f) Cycling performance, coulomb efficiency, and (inset) SEM image of ALC-700 with a current density of 1 A $g^{-1}$ after 10000 cycles in a three-electrode system.

is superior to those of the two other ALCs, thus revealing differences in specific surface areas and hydrophilicity caused by heat treatment (Table S2) [51]. The pseudocapacitance of ALC-700 was also better than that of CAJ (Fig. S7), thus showing the remarkable theoretical specific capacitance of functional $Co_3O_4$. The specific capacitances of ALC-700 calculated from the GCD curves (Fig. 3d) at current densities of 1, 2, 4, 8, 12, and 20 A $g^{-1}$ are 1345.2, 1206.4, 1035.2, 867.2, 758.4, and 656 F $g^{-1}$, respectively. As known to us, micropores and most mesopores below ~5 nm will lose their activities [52]. Otherwise mass transport may be a key factoring influencing diffusion inside an electrode at a high current density. The 3D net-like microstructure with hierarchical pores of 5–50 nm allows effective utilization of electroactive sites, provides fast mass transport in three dimensions, and accommodates the strain of volume change during the charge/discharge process.

Ionic transport in different electrodes was evaluated by EIS in the frequency range of $10^{-2}$–$10^{5}$ Hz (Fig. 3e). In general, a low equivalent series resistance (ESR) indicates a low internal contact resistance and a rapid charge–discharge rate [1,17]. The inset in Fig. 3e indicates an equivalent circuit possessing a combination of parameters, including a resistance $R_s$ (ionic resistance of the electrode and contact resistance at the active material/current collector interface), the charge transfer $R_{ct}$ (semicircle diameter), and a Warburg resistance $Z_W$ (ion diffusion/transport from the electrolyte to the electrode surface) [53]. The ESR of ALC-700 (0.54 Ω) was lower than that of the other ALCs and bare $Co_3O_4$ (0.72 Ω), thus suggesting that the carbon matrix functions as an effective conductive substrate to reduce the contact resistance of the interface. The smallest $R_s$ and $R_{ct}$ of ALC-700 indicated that the 3D hierarchical structure could establish good electron transport and ion diffusion pathways. Moreover, the surface wettability of the sample, which is ascribed to the N and O functional groups retained from aloe, promotes direct contact between the electrode material and electrolyte, the rapid formation of the EDLC, and reversible Faradaic reactions. The cycling stability and Coulombic efficiency of the hierarchical structures of ALC-700 were evaluated under GCD conditions (Fig. 3f). ALC-700 showed a specific capacitance of 92.7% of its initial value, a Coulombic efficiency of 95.8%, and nearly the same porous morphology (inset in Fig. 3f) after 10000 cycles, thus suggesting its excellent cycling stability.

An ASC was also assembled using ALC-700 and active carbon (AC) electrodes with KOH as the aqueous electrolyte (Fig. 4a). The as-fabricated cell had a wide potential window of 0–1.5 V (Fig. 4b and S8), which is 0–0.6 V in a three-electrode system (Fig. 3a). In Fig. 4c, the CV curves of the device showed similar profiles under different scan rates, thus exhibiting good reversibility. The specific capacitance of the capacitor was 446.5 F $g^{-1}$ at 2 A $g^{-1}$ (Fig. 4d). The power and energy densities of the ASCs were calculated from the GCD curves at various current densities based on the following equations:

$$E = CV^2/2 \quad (4)$$

$$P = E/\Delta t, \quad (5)$$

where E is the specific energy density (Wh·$kg^{-1}$) and P is the power density (W·$kg^{-1}$). Fig. 4e shows the Ragone plots of the ASC consisting of different electrodes. Among the hybrid supercapacitors, the ALC-700//AC ASC delivered a maximum energy density of 68.17 Wh·$kg^{-1}$ at a power density of 549 W·$kg^{-1}$ and maintained an energy density of 21.39 Wh·$kg^{-1}$ at 5.5 kW·$kg^{-1}$; these values are comparable with or even higher than those of state-of-the-art ASCs [54–60]. A specific capacitance of about 87.92% of the original value was retained in the cell after 10000 cycles (Fig. 4f), which suggests that the electrode possesses excellent recyclability. The energy densities of the as-assembled ASC

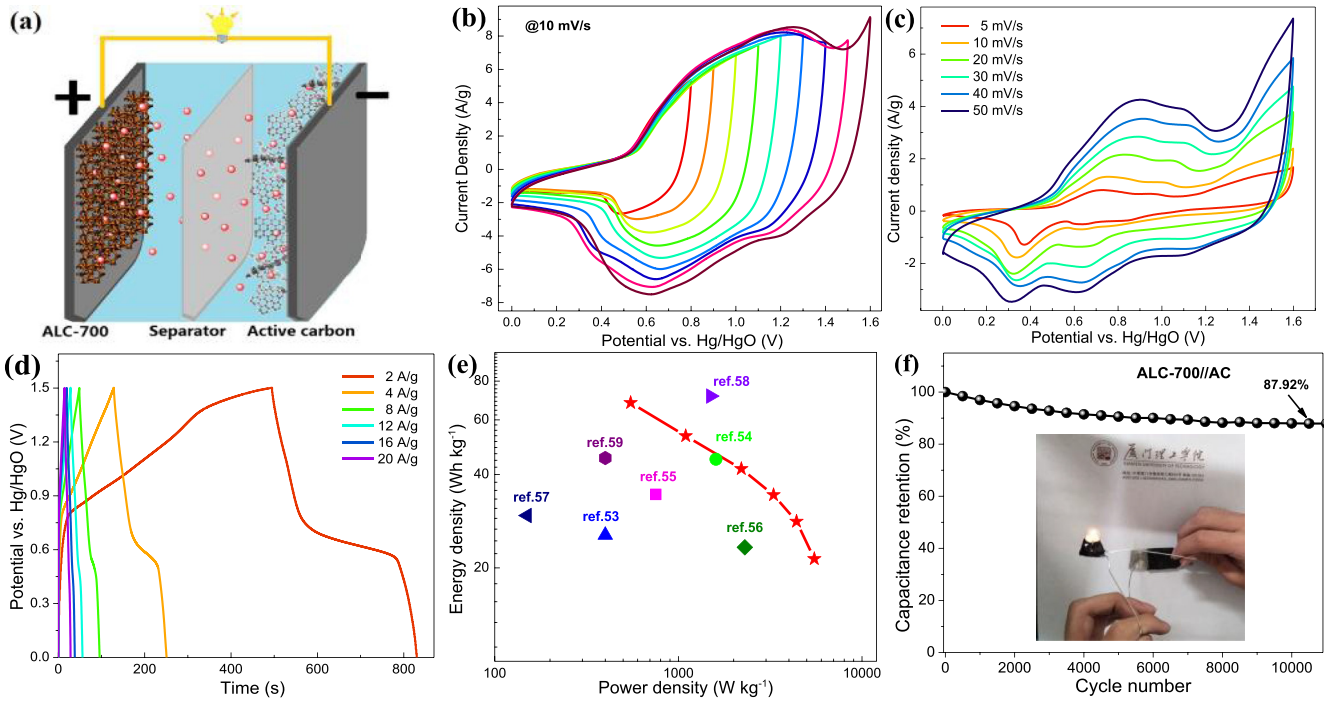


**Fig. 4.** (a) Configuration of the asymmetric supercapacitor based on an ALC-700 anode and AC cathode with 6 M KOH electrolyte in a two-electrode system. CV curves of the ALC-700//AC electrodes tested at (b) different voltage windows and (c) various scan rates. (d) GCD curves of the as-assembled ASC measured at different current densities. (e) Ragone plots relating the energy and power densities of the ASC device compared with literature results. (f) Changes in the capacitance retention of the ALC-700//AC ASC as a function of cycle number (inset is the demo).

device are much larger than those of many other electrodes; such a feature is mainly attributed to the wide operating voltage window of the fabricated devices. Two ASC devices in series can effectively provide 3.0 V to operate a red light-emitting diode (LED) (inset in Fig. 4f) for about 3 min after charging for 200 s at 2 A $g^{-1}$.

The supercapacity of the as-prepared ALCs is superior to those of many other reported $Co_3O_4$-based composites (Table S3) [50–55]. The as-prepared products are thus expected to demonstrate remarkable electrochemical properties owing to the unique characteristics of their microstructure. First, numerous $Co_3O_4$ nanocrystals of ~10 nm in diameter (Fig. 1f) coated on a net-like carbon skeleton with a high conductivity show excellent dispersion, thus suggesting enhanced utilization of electroactive sites and a promising theoretical pseudocapacitance of the electrode. Second, the 3D net-like architecture formed by hierarchical pores measuring several dozen nanometers demonstrates that the electrolyte can easily diffuse through the active electrode material [17,50]. Furthermore, the proposed bio-derived carbon network promotes the electronic conductivity of the ALCs effectively and can provide a pathway for charges, resulting in better performance and excellent stability of the capacitor.

## 4. Conclusion

Novel 3D net-like $Co_3O_4$/C composites assembled from $Co_3O_4$ nanocrystals and a carbon aerogel matrix derived from CAJ were successfully fabricated via an effective solvothermal route. ALC-700 exhibited a specific capacity of 1345.2 F $g^{-1}$ at 1 A $g^{-1}$ and retained a capacity of 92.7% and a coulombic efficiency of 95.8% after 10000 cycles; these values are 30 times higher than that of $Co_3O_4$. The fabricated electrode can also maintain its original morphology without severe breakage after the GCD process, thereby exhibiting excellent cyclability. The ASC device assembled from ALC-700 and AC delivered a high energy density of 68.17 Wh·$kg^{-1}$ at a power density of 549 W·$kg^{-1}$. Moreover, the device exhibited superior cycling stability and retained 87.92% of the original capacitance after 10000 cycles. Utilization of aloe vera presents a novel approach for the use of natural juice-derived carbon sources as controllable electrode materials in energy conversion and storage devices. The synthetic pathway proposed in this work could provide a unique strategy to fabricate promising nano/micro-functional materials via a simple and low-cost process using natural templates.

## Acknowledgements

Qinwen Yin and Liwen He contributed equally to this work. This work was supported by the Natural Science Foundation of Fujian Province of China (2014H0028 and 11204258), Outstanding Young Scientific Research Personnel Training Plan in Colleges and Universities of Fujian Province (JA13229), the Open Fund of Fujian Provincial Key Laboratory of Functional Materials and Applications (Xiamen University of Technology) and Educational Research Projects for Young and Middle-aged Teachers in Fujian (JT180422).

## Appendix A. Supplementary data

Supplementary data to this article can be found online at https://doi.org/10.1016/j.carbon.2019.08.060.

## References

[1] P. Simon, Y. Gogotsi, Materials for electrochemical capacitors, Nat. Mater. 7 (11) (2008) 845–854.
[2] H.G. Zhang, X.D. Yu, P.V. Braun, Three-dimensional bicontinuous ultrafast-charge and -discharge bulk battery electrodes, Nat. Nanotechnol. 6 (2011) 277–281.
[3] X. Yang, H. Li, A.Y. Lu, S. Min, Z. Idriss, M.N. Hedhili, et al., Highly acid-durable carbon coated $Co_3O_4$ nanoarrays as efficient oxygen evolution electrocatalysts,

Nano Energy 7 (25) (2016) 42–45.
[4] X. Cao, Z. Yin, H. Zhang, Three-dimensional graphene materials: preparation, structures and application in supercapacitors, Energy Environ. Sci. 7 (2014) 1850–1865.
[5] D. Sheberla, J.C. Bachman, J.S. Elias, C.J. Sun, Y. Shao-horn, M. Dincă, Conductive MOF electrodes for stable supercapacitors with high areal capacitance, Nat. Mater. 16 (2) (2017) 220–224.
[6] Z.Y. Yu, L.F. Chen, L.T. Song, Y.W. Zhu, H.X. Ji, S.H. Yu, Free-standing boron and oxygen co-doped carbon nanofiber films for large volumetric capacitance and high rate capability supercapacitors, Nano Energy 15 (7) (2015) 235–243.
[7] Q. Liao, N. Li, S. Jin, G. Yang, C. Wang, All-Solid-state symmetric supercapacitor based on $Co_3O_4$ nanoparticles on vertically aligned graphene, ACS Nano 9 (5) (2015) 5310–5317.
[8] B. Liu, D. Kong, J. Zhang, Y. Wang, T. Chen, C. Cheng, et al., 3D hierarchical $Co_3O_4$@$Co_3S_4$ nanoarrays as cathode materials for asymmetric pseudocapacitors, J. Mater. Chem. 4 (9) (2016) 3287–3296.
[9] R. Na, X. Wang, N. Lu, G. Huo, H. Lin, G. Wang, Novel egg white gel polymer electrolyte and a green solid-state supercapacitor derived from the egg and rice waste, Electrochim. Acta 274 (6) (2018) 316–325.
[10] R.R. Gaddam, D. Yang, R. Narayan, K. Raju, N.A. Kumar, X.S. Zhao, Biomass derived carbon nanoparticle as anodes for high performance sodium and lithium ion batteries, Nano Energy 26 (8) (2016) 346–352.
[11] Y. Lu, L. Yu, M. Wu, Y. Wang, X.W. Lou, Construction of complex $Co_3O_4$@$Co_3V_2O_8$ hollow structures from metal–organic frameworks with enhanced lithium storage properties, Adv. Mater. 30 (1) (2018) 1702875.
[12] L. Zhang, H.B. Wu, Y. Yan, X. Wang, X.W. Lou, Hierarchical $MoS_2$ microboxes constructed by nanosheets with enhanced electrochemical properties for lithium storage and water splitting, Energy Environ. Sci. 7 (10) (2014) 3302–3306.
[13] B. Wu, Y. Xie, Y. Meng, C. Qian, Y. Chen, A. Yuan, et al., Constructing unique heterogeneous cobalt-manganese oxideporous microspheres as anode for long-cycle and high-rate lithium ion batteries, J. Mater. Chem. 7 (11) (2019) 6149–6160.
[14] D. Sun, L. He, R. Chen, Y. Liu, B. Lv, S. Lin, et al., Biomorphic composites composed of octahedral $Co_3O_4$ nanocrystals and mesoporous carbon microtubes templated from cotton for excellent supercapacitor electrodes, Appl. Surf. Sci. 465 (2019) 232–240.
[15] K. Yu, X. Pan, G. Zhang, X. Liao, X. Zhou, M. Yan, et al., Nanowires in energy storage devices: structures, synthesis, and applications, Adv. Energy Mater. 8 (2018) 1802369.
[16] G.J. Wei, Z. Zhou, X.X. Zhao, W.Q. Zhang, C.H. An, Ultrathin metal-organic framework nanosheet-derived ultrathin $Co_3O_4$ nanomeshes with robust oxygen-evolving performance and asymmetric supercapacitors, ACS Appl. Mater. Interfaces 10 (28) (2018) 23721–23730.
[17] D. Sun, L. He, R. Chen, Z. Lin, S. Lin, C. Xiao, et al., The synthesis, characterization and electrochemical performance of hollow sandwich microtubules composed of ultrathin $Co_3O_4$ nanosheets and porous carbon using a biotemplate, J. Mater. Chem. 9 (36) (2018) 18987–18993.
[18] X. Wang, W. Tian, T. Zhai, C. Zhi, Y. Bando, D. Golberg, Cobalt(II,III) oxide hollow structures: fabrication, properties and applications, J. Mater. Chem. 22 (44) (2012) 23310–23326.
[19] B. Liu, H. Liu, M. Liang, L. Liu, Z. Lv, Z.H. hou, et al., Controlled synthesis of hollow octahedral $ZnCo_2O_4$ nanocages assembled by untrathin 2D nanosheets for enhanced lithium storage, Nanoscale 9 (44) (2017) 17174–17180.
[20] A. Kumar, N. Kumar, P. Baredar, A. Shukla, A review on biomass energy resources, potential, conversion and policy in India, Renew. Sustain. Energy Rev. 45 (2015) 530–539.
[21] D.V. Kosynkin, A.L. Higginbotham, A. Sinitskii, J.R. Lomeda, A. Dimiev, B.K. Price, et al., Longitudinal unzipping of carbon nanotubes to form graphene nanoribbons, Nature 458 (2009) 872–876.
[22] J. Yang, H. Sun, H. Liang, H. Ji, L. Song, C. Gao, et al., A highly efficient metal-free oxygen reduction electrocatalyst assembled from carbon nanotubes and graphene, Adv. Mater. 28 (23) (2016) 4606–4613.
[23] Y. Zheng, Z. Li, J. Xu, T. Wang, X. Liu, X. Duan, et al., Multi-channeled hierarchical porous carbon incorporated $Co_3O_4$ nanopillar arrays as 3D binder-free electrode for high performance supercapacitors, Nano Energy 20 (2016) 94–107.
[24] D. Sun, L. He, Y. Lai, J. Lian, J. Sun, A. Xie, et al., Structure and electrochemical properties of $Mn_3O_4$ nanocrystal-coated porous carbon microfiber derived from cotton, Materials 11 (2018) 1987.
[25] P. Zhang, Z. Zhao, B. Dyatkin, C. Liu, J. Qiu, In situ synthesis of cotton-derived Ni/C catalysts with controllable structures and enhanced catalytic performance, Green Chem. 18 (12) (2016) 3594–3599.
[26] C. Qian, X. Guo, W. Zhang, H. Yang, Y. Qian, F. Xu, et al., $Co_3O_4$ nanoparticles on porous bio-carbon substrate as catalyst for oxygen reduction reaction, Microporous Mesoporous Mater. 277 (2019) 45–51.
[27] X.X. Wang, D.A. Cullen, Y.T. Pan, S. Hwang, M. Wang, Z. Feng, et al., Nitrogen-coordinated single cobalt atom catalysts for oxygen reduction in proton exchange membrane fuel cells, Adv. Mater. 30 (11) (2018) 1706745.
[28] Z. Wang, D. Shen, C. Wu, S. Gu, State-of-the-art on the production and application of carbon nanomaterials from biomass, Green Chem. 20 (22) (2018) 5031–5057.
[29] Y. Zhu, M. Chen, Q. Li, C. Yuan, C. Wang, A porous biomass-derived anode for high-performance sodium-ion batteries, Carbon 129 (2018) 695–701.
[30] V. Sahu, R.B. Marichi, G. Singh, R.K. Sharma, Hierarchical polyaniline spikes over vegetable oil derived carbon aerogel for solid-state symmetric/asymmetric supercapacitor, Electrochim. Acta 240 (6) (2017) 146–154.
[31] Y. Zhang, Z. Gao, N. Song, X. Li, High-performance supercapacitors and batteries derived from activated banana-peel with porous structures, Electrochim. Acta 22 (12) (2016) 1257–1266.
[32] T.L. Lee, R.A. Adams, C. Luhrs, A. Arora, V.G. Pol, C.H. Wu, et al., High-stability tin/carbon battery electrodes produced using reduction expansion synthesis, Carbon 132 (2018) 411–419.
[33] Y. Liu, B. Lv, P. Li, Y. Chen, B. Gao, B. Lin, Biotemplate-assisted hydrothermal synthesis of tubular porous $Co_3O_4$ with excellent charge-discharge cycle stability for supercapacitive electrodes, Mater. Lett. 210 (1) (2018) 231–234.
[34] X. Zhou, F. Cao, J. Li, W. Shen, J. Liu, Synthesis of porous $Co_3O_4$/C/[Mg, Ca]O nanocomposites by natural biological template for application in dynamic damping absorption, J. Alloy. Comp. 688 (2016) 354–361.
[35] J. Deng, M. Li, Y. Wang, Biomass-derived carbon: synthesis and applications in energy storage and conversion, Green Chem. 18 (18) (2016) 4824–4854.
[36] P. Haldar, S. Biswas, V. Sharma, A. Chowdhury, A. Chandra, $Mn_3O_4$-polyaniline-graphene as distinctive composite for use in high-performance supercapacitors, Appl. Surf. Sci. 491 (2019) 171–179.
[37] D.P.M.D. Shaik, R. Pitcheri, Y. Qiu, O.M. Hussain, Hydrothermally synthesized porous $Mn_3O_4$ nanoparticles with enhanced electrochemical performance for supercapacitors, Ceram. Int. 45 (2019) 2226–2233.
[38] L. Jiang, D. Luo, Q. Zhang, S. Ma, G. Wan, X. Lu, et al., Electrochemical performance of free-standing and flexible graphene and $TiO_2$ composites with different conductive polymers as electrodes for supercapacitors, Chem. Eur J. (2019). https://doi.org/10.1002/chem.201900399.
[39] Y. Jiang, X. Yan, Y. Cheng, Y. Zhang, W. Xiao, L. Gan, et al., A general method to fabricate $MoO_3$/C composites and porous C for asymmetric solid-state supercapacitors, RSC Adv. 9 (2019) 13207–13213.
[40] V.K. Patel, S. Bhattacharya, High-performance nanothermite composites based on aloe-vera-directed CuO nanorods, ACS Appl. Mater. Interfaces 5 (24) (2013) 13364–13374.
[41] P. Jithendra, A.M. Rajam, T. Kalaivani, A.B. Mandal, C. Rose, Preparation and characterization of aloe vera blended collagen-chitosan composite scaffold for tissue engineering applications, ACS Appl. Mater. Interfaces 5 (15) (2013) 7291–7298.
[42] J. Liang, Y. Jiao, M. Jaroniec, S.Z. Qiao, Sulfur and nitrogen dual-doped mesoporous graphene electrocatalyst for oxygen reduction with synergistically enhanced performance, Angew. Chem. Int. Ed. 51 (2012) 11496–11500.
[43] S. Zhou, G. Chen, X. Feng, M. Wang, T. Song, D. Liu, et al., In situ $MnO_x$/N-doped carbon aerogels from cellulose as monolithic and highly efficient catalysts for the upgrading of bioderived aldehydes, Green Chem. 20 (15) (2018) 3593–3603.
[44] F.L. Lai, Y.L. Miao, L.Z. Zuo, H.Y. Lu, Y.P. Huang, T.X. Liu, Biomass-derived nitrogen-doped carbon nanofiber network: a facile template for decoration of ultrathin nickel-cobalt layered double hydroxide nanosheets as high-performance asymmetric supercapacitor electrode, Small 12 (24) (2016) 3235–3244.
[45] D. Yan, H. Zhang, L. Chen, G. Zhu, S. Li, H. Xu, et al., Biomorphic synthesis of mesoporous $Co_3O_4$ microtubules and their pseudocapacitive performance, ACS Appl. Mater. Interfaces 6 (2014) 15632–15637.
[46] Y. Lv, L. Gan, M. Liu, W. Xiong, Z. Xu, D. Zhu, et al., A self-template synthesis of hierarchical porous carbon foams based on banana peel for supercapacitor electrodes, J. Power Sources 209 (7) (2012) 152–157.
[47] L.G. Cancado, A. Jorio, E.H. Ferreira, C.A. Achete, R.B. Capaz, B. Moutinho, et al., Quantifying defects in graphene via Raman spectroscopy at different excitation energies, Nano Lett. 11 (8) (2011) 3190–3196.
[48] W.L. Earl, Y.W. Kim, D.M. Smith, Characterization of porous solids III, Pure Appl. Chem. 66 (2006) 1739–1758.
[49] G. Zan, Q. Wu, Biomimetic and bioinspired synthesis of nanomaterials/nanostructures, Adv. Mater. 28 (11) (2016) 2099–2149.
[50] Q. Lu, J.G. Chen, J.Q. Xiao, Nanostructured electrodes for high-performance pseudocapacitors, Angew. Chem. Int. Ed. 52 (7) (2013) 1882–1889.
[51] Z. Li, X. Liu, L. Wang, F. Bu, J. Wei, D. Pan, et al., Hierarchical 3D all-carbon composite structure modified with N-doped graphene quantum dots for high-performance flexible supercapacitors, Small 14 (2018) 1801498.
[52] Y. Wang, Y. Song, Y. Xia, Electrochemical capacitors: mechanism, materials, systems, characterization and applications, Chem. Soc. Rev. 45 (21) (2016) 5925–5950.
[53] Y. Gogotsi, P. Simon, True performance metrics in electrochemical energy storage, Science 334 (2011) 917–918.
[54] C. Lai, Y. Sun, X. Zhang, H. Yang, W. Kang, B. Lin, Advanced flower-like $Co_3O_4$ with ultrathin nanosheets and 3D rGO aerogels as double ion-buffering reservoirs for asymmetric supercapacitors, Electrochim. Acta 271 (6) (2018) 379–387.
[55] Y. Zou, C. Cai, C. Xiang, P. Huang, H. Chu, Z. She, et al., Simple synthesis of core-shell structure of Co–$Co_3O_4$@carbon-nanotube-incorporated nitrogen-doped carbon for high-performance supercapacitor, Electrochim. Acta 261 (1) (2018) 537–547.
[56] M. Zhu, Q. Chen, J. Kan, J. Tang, W. Wei, J. Lin, et al., Cobalt oxide nanoparticles embedded in N-doped porous carbon as efficient electrode for supercapacitor, Small (2019), https://doi.org/10.1002/ente.201800963.
[57] M. Qorbani, T.C. Chou, Y.H. Lee, S. Samireddi, N. Naseri, A. Ganguly, et al., Multi-porous $Co_3O_4$ nanoflakes@sponge-like few-layer partially reduced graphene oxide hybrids: towards highly stable Asymmetric supercapacitors,

J. Mater. Chem. 5 (24) (2017) 12569–12577.
[58] J. Li, G. Zan, Q. Wu, An ultra-high-performance anode material for supercapacitors: self-assembled long $Co_3O_4$ hollow tube network with multiple heteroatom [C-, N- and S-] doping, J. Mater. Chem. 4 (23) (2016) 9097–9105.
[59] T. Zhai, L.M. Wan, S. Sun, Q. Chen, J. Sun, Q.Y. Xia, et al., Phosphate ion functionalized $Co_3O_4$ ultrathin nanosheets with greatly improved surface reactivity for high performance pseudocapacitors, Adv. Mater. 29 (7) (2017) 1604167.
[60] J. Wang, X. Zhang, Q.L. Wei, H.M. Lv, Y.L. Tian, Z.Q. Tong, et al., 3D self-supported nanopine forest-like $Co_3O_4$@$CoMoO_4$ core-shell architectures for high-energy solid state supercapacitors, Nano Energy 19 (1) (2016) 222–233.